A&A, 709, A231 (2026)
https://doi.org/10.1051/0004-6361/202558329

Astronomy & Astrophysics

Chemically peculiar candidates in 18 Milky Way globular clusters

M. Špoková[1,2,⋆], M. Skarka[1,2], Z. Prudil[3], E. Paunzen[1], F. Hroch[1], and V. Glos[1]

[1] Department of Theoretical Physics and Astrophysics, Masaryk University, Kotlářská 2, 60200 Brno, Czech Republic
[2] Astronomical Institute of Czech Academy of Sciences, Fričova 298, 251 65 Ondřejov, Czech Republic
[3] European Southern Observatory, Karl-Schwarzschild-Strasse 2, 85748 Garching bei München, Germany

Received 1 December 2025 / Accepted 31 March 2026

ABSTRACT

Context. Recent discoveries show that chemically peculiar (CP) stars also reside in globular clusters (GCs). The channels leading to chemical peculiarity are, however, still under discussion.
Aims. The main goals of our investigation are to identify the CP stars in GCs and search for systematic relations among different stellar groups commonly observed in GCs and chemical peculiarity. Additionally, we search for possible correlations of the occurrence rate of CP stars with the cluster properties.
Methods. We obtained *BVg2* multicolour photometry for 18 southern GCs with the 1.54 m Danish telescope located at La Silla observatory in Chile. The data were reduced and processed with standard IRAF tools. To avoid blending, we omitted central parts of the clusters. We determined the membership of the stars to a particular GC based on the proper motion and parallax of the stars from the Gaia DR3 catalogue. Colour-magnitude diagrams were constructed, and only stars on horizontal branch and in the region of blue stragglers were considered for further analysis. Construction of the Δa diagram allowed us to identify CP candidate stars with high probability. To test the reliability of our approach, we used spectroscopic observations of M53.
Results. Except for four GCs, CP candidates were found in all other GCs with the average fraction of 4.2%. We found that a significant portion of the candidates are blue stragglers. These constitute a full sample of identified CP candidates in four GCs and represent more than 60% of the candidates in ten GCs.
Conclusions. The a photometry was found as a powerful tool for the identification of CP stars in GCs. We discovered a possible connection between chemical peculiarity and blue straggler stars.

Key words. blue stragglers – stars: chemically peculiar – stars: horizontal-branch – globular clusters: general

1. Introduction

Globular clusters (GCs) are among the oldest objects in our Galaxy. They are gravitationally bound assemblies of up to a million stars. Previously thought to be of a uniform population, now we know that their structure and composition are more complex (Milone & Marino 2022), as we are finding multiple stellar populations present in them; for example, an extreme case of ω Cen (Tailo et al. 2016).

Presumably much larger in the past, these objects have been enriching the field star population through the gradual loss of members due to dynamical effects during their orbits around the Galactic centre (Piatti & Carballo-Bello 2020). In our Galaxy, there are about 160 GCs. Some of these formed in situ, while others were accreted and are associated with known merger events and stellar streams (Massari et al. 2019; Massari 2025). Differences in origin can result in an overall anomalous chemical composition (depletion of Mn, Si, and Ca, and a difference in Zn and Eu) between accreted clusters and those formed in situ (Ceccarelli et al. 2024)

In GCs, we can find stars in an environment different from that of the Galactic field. According to Gratton et al. (2012), we can observe star-to-star abundance variations in light elements (C, N, O, Na, Mg, and Al) in GCs, possibly caused by their membership of different stellar populations. Also, carbon-enhanced stars, CH and CN-strong stars, have been observed in GCs, and in massive clusters, helium-enriched populations may be present along the extreme horizontal branch (EHB). Behr et al. (1999) and Pace et al. (2006) detected super-solar abundances of iron in horizontal-branch (HB) stars in M 13 and NGC 2808, respectively. Michaud et al. (2008) confirmed that atomic diffusion may play a role in HB stars and can explain the overabundance of Fe and other elements. Momany et al. (2020) studied EHB subdwarfs that commonly occur in binary systems in the field but are not observed in binaries within GCs. While investigating these stars, they found $\alpha 2$ Canum-Venaticorum-type photometric variability present in the fraction of GCs' EHB stars.

This type of variability is commonly found among hot main-sequence stars that exhibit a non-uniform distribution of chemical elements on their surfaces (Michaud et al. 1981; Bernhard et al. 2015), leading to flux redistribution across the stellar surface (Krtička et al. 2013). As the star rotates, these chemically distinct surface regions, sustained by strong magnetic fields, produce photometric variability, as explained by the oblique rotator model (Stibbs 1950). Chemically peculiar (CP) stars with strong magnetic fields form a distinct class known as CP2, Ap/Bp, or ACV stars (Preston 1974).

Generally, chemical peculiarity emerges in stars exhibiting slow rotation and calm atmospheres (Michaud et al. 1976). Under these conditions, radiative levitation and/or gravitational settling can occur, leading to surface abundance anomalies (for example, overabundance of Mn, Sr, Y, and rare earth elements, Michaud 1970; Hümmerich et al. 2020). If the magnetic field is present, stable chemical spots can appear on the surface of CP stars and create a rotationally variable object of a CP2 nature.

⋆ Corresponding author: 393635@mail.muni.cz

Strong magnetic fields are also common in He-weak stars (CP4 class, Preston 1974). There are also CP stars that do not show magnetic fields. First, the CP1 contains metallic Am-Fm stars that show an under-abundance of Ca and Sc and an overabundance of Fe-peak elements (Preston 1974; Michaud et al. 1983). Non-magnetic stars in the CP3 class show a strong overabundance of Hg and Mn that can be of the order of a few magnitudes compared to the Sun (Preston 1974; Ghazaryan & Alecian 2016). The last class of CP stars without strong magnetic fields are λ Bootis stars. They show solar abundances of C, N, O and S but are metal-poor (Gray 1988; Paunzen 1998).

The origin of magnetic fields in CP2 stars remains an open question. Two primary mechanisms have been proposed: either the magnetic field is of a fossil origin, preserved from the time of stellar formation (e.g. Braithwaite & Spruit 2004), or it is generated during a stellar merger event (e.g. Ferrario 2018; Schneider et al. 2019). The merger scenario, which could partially explain the absence of CP2 stars in close binaries, has been discussed by Ferrario et al. (2009), Tutukov & Fedorova (2010), and Schneider et al. (2016). This scenario is also thought to contribute to the formation of blue straggler stars (BSs), which are commonly observed in GCs.

CP stars can be effectively identified by photometry using dedicated filters covering regions with a number of absorption lines that produce a flux depression in these regions (Kodaira 1969). One such region, around 5200 Å, is covered by the $g2$ filter (Maitzen 1998). The flux in this part of the spectrum is then compared with the flux in the adjacent regions. In this work, we used it in combination with Johnson B and V filters to perform a photometry (Maitzen et al. 1998). This method has been used to identify stars in open clusters and stellar fields (e.g., Cariddi et al. 2018; Netopil et al. 2007; Paunzen et al. 2014b) but also in GCs (Paunzen et al. 2014a). The method is particularly efficient at identifying magnetic CP2 and CP4 stars[1], less efficient for the identification of λ Boo stars, and not sensitive enough to identify CP1 and CP3 stars (Paunzen et al. 2005).

Paunzen et al. (2014b) investigated the three GCs NGC 104, NGC 6205, and NGC 7099 and found that about 3 percent of the stars lie in abnormal regions in the diagnostic diagrams. This could be taken as a guideline. However, after this finding, no new analysis in that respect was conducted.

We analysed 18 GCs. The data reduction process is described in Sect. 2, and the methodology and validation of the a-photometry technique are presented in Sect. 3. We find that the majority of chemically peculiar candidates (CPCs) identified are BSs. This result, along with statistical analysis, is discussed in Sect. 4.

2. Data and methodology

In the following section, we describe the target selection and observational set-up, and outline the data processing procedure, including membership analysis and the selection of regions used for further analysis.

2.1. Data sample and observations

We selected GCs based on their observability from La Silla, Chile, and their observation characteristics. We considered their brightness (<10 mag) and angular size (>5′). These parameters are crucial to obtain reasonable data and at least partially eliminate contamination in the crowded fields of GCs by targeting the spatially largest GCs.

Our GC sample consists of systems with a broad range of metallicities, from −2.06 to −0.45 (Carretta et al. 2009). The age distribution lies in the interval from 11 to 13 Gyr. The origin of GCs might play a significant role in determining their chemical composition; for example, in the known depletion of certain chemical elements (Ceccarelli et al. 2024). Therefore, for the purpose of further analysis of our GC sample, clusters were also marked by their presumed origin – whether they formed in situ or are associated with a known merger or stellar stream. This classification was based on their dynamical properties as estimated by Massari et al. (2019), Massari (2025) via Gaia DR2 and DR3 data analysis.

During the years 2019–2020, we managed to observe 23 GCs. Photometric data were acquired using the 1.54 m Danish telescope located at the La Silla Observatory, Chile, employing the DFOSC 2048 × 2048 CCD imager, which provides a square field of view of 13.5 × 13.5 arcmin with a spatial resolution of 0.396 arcsec/px. From this set, data for some GCs were not suitable for analysis due to poor quality. After an initial review, we decided to perform a photometry (see following Sect. 3) on 18 selected GCs. The basic parameters of the studied GCs are listed in Table 1.

The GCs were observed in Johnson B and V filters (90 s and 40 s exposure times, respectively), and Maitzen's $g2$ filter (180 s exposure; Johnson & Morgan 1953; Maitzen 1976). For each GC, at least two observations were made in each filter to improve the signal-to-noise ratio (S/N).

2.2. Basic data processing

Cosmic ray hits, and flat-field and bias corrections, were performed using the `Munipack`[2] package (Hroch 2014). This software was also used to stack the individual frames. Due to vignetting effects, the outer regions of each GC image were masked using the main background noise value. This masking was carried out with the `AstroPy` library (Astropy Collaboration 2013, 2018, 2022).

The point spread function (PSF) photometry was then performed in `IRAF` using the `DAOPHOT` package for crowded field photometry (Stetson 1987). Workflow and magnitude error estimates were adopted exactly as recommended in (Davis 1994).

To maintain control over the construction of the PSF, the stars for each GC were manually selected in `IRAF`. For each cluster, we selected at least 20 well-defined stars without saturated pixels or close neighbours to ensure an accurate PSF model. The PSF that best described the stellar profiles in our data was the Moffat function with $\beta = 2.5$ (`moffat25` in `IRAF`; Moffat 1969). A typical PSF radius was 3.6 px.

The stars photometrically identified in different filters were cross-matched using `TOPCAT` (Thompson 2005). Only stars detected in all filters and matched within a maximum tolerance of 1 arcsec were retained for further analysis. While the broad Johnson filter frames contained several thousand to tens of thousands of stars, the narrower $g2$ filter posed a limitation, but still provided typically several hundred to a few thousand stars.

Because of heavy crowding in the central regions of GCs, photometric measurements in those areas are often unreliable. Therefore, we excluded the cluster cores from the analysis by applying a flux profile-based masking procedure. We used 10 sigma above the background level as the threshold limit. We

[1] Line blanketing of iron-group and earth-rare elements is strengthened by magnetic fields.

[2] Available at `https://munipack.physics.muni.cz/docs.html`

Table 1. Observed targets.

ID	RA	DEC	V [mag]	M [$\times 10^5\ M_\odot$]	R_S [kpc]	D [′]	Fe/H	Age [Gyr]	Origin
NGC 1851	05:14:06.76	−40:02:47.6	7.07	2.83	11.95	12	−1.18	11.00[1]	G-E
NGC 2808	09:12:03.10	−64:51:48.6	6.13	7.91	10.06	14	−1.18	11.00[1]	G-E
NGC 3201	10:17:36.82	−46:24:44.9	6.77	1.93	4.74	20	−1.51	11.50[1]	Seq/G-E
NGC 4833	12:59:33.92	−70:52:35.4	7.19	1.86	6.48	14	−1.89	12.50[1]	G-E
NGC 5024	13:12:55.25	+18:10:05.4	7.70	5.02	18.50	13	−2.06	12.25[1]	H99
NGC 5272	13:42:11.62	+28:22:38.2	6.39	4.09	10.18	18	−1.50	11.75[1]	H99
NGC 5904	15:18:33.22	+02:04:51.7	5.95	3.93	7.48	23	−1.33	11.50[1]	H99/G-E
NGC 6121	16:23:35.22	−26:31:32.7	5.65	9.04	1.85	36	−1.18	11.50[1]	L-E
NGC 6218	16:47:14.18	−01:56:54.7	7.09	1.08	5.11	16	−1.33	13.00[1]	M-D
NGC 6254	16:57:09.05	−04:06:01.1	6.61	1.89	5.07	20	−1.57	11.75[1]	L-E
NGC 6266	17:01:12.80	−30:06:49.4	5.65	0.90	1.85	15	−1.18	11.78[2]	M-B
NGC 6273	17:02:37.80	−26:16:04.7	6.88	7.20	8.34	17	−1.76	11.90[2]	L-E
NGC 6388	17:36:17.23	−44:44:07.8	6.82	13.10	11.17	10	−0.45	12.03[2]	M-B
NGC 6397	17:40:42.09	−53:40:27.6	5.45	0.82	2.48	31	−1.99	13.00[1]	M-D
NGC 6402	17:37:36.10	−03:14:45.3	7.87	6.00	9.14	11	−1.39	12.50[2]	L-E
NGC 6541	18:08:02.36	−43:42:53.6	6.61	2.57	7.61	15	−1.82	12.50[1]	L-E
NGC 6656	18:36:23.94	−23:54:17.1	5.06	4.7	3.30	32	−1.70	12.50[1]	M-D
NGC 6723	18:59:33.15	−36:37:56.1	7.21	1.97	8.27	13	−1.10	12.50[1]	M-B

Notes. Columns are defined as follows: ID gives the NGC catalogue identification number, RA and DEC give celestial coordinates in hexadecimal format, V is the Johnson magnitude, M gives mass, and R_S is distance from the Sun. The values were adopted from (Baumgardt et al. 2023). D is the angular size on the sky, taken from (Frommert & Kronberg 2019). Fe/H is a metallicity as estimated in (Carretta et al. 2009). Age values marked with [1] taken from (VandenBerg et al. 2013) and values marked [2] from (Forbes & Bridges 2010). Origin gives the dynamical origin of the clusters as estimated by (Massari et al. 2019). Abbreviations in this column were adopted from the above-mentioned work as follows: M-D for Main-Disc; M-B for Main-Bulge; G-E for Gaia-Enceladus; H99 for Helmi Streams; Seq for Sequoia galaxy; and L-E for clusters unassociated with any of the stellar streams but exhibiting low energy.

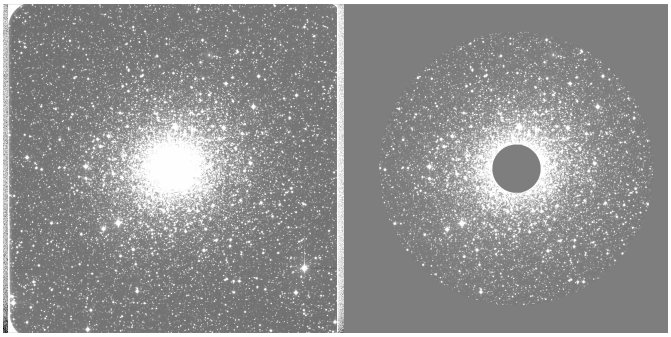

Fig. 1. Illustration of masking. Raw image of NGC 6541 (left) and the same frame with applied mask covering vignetting region as well as the overcrowded central part of the cluster.

adopted this threshold after manual tests to ensure a consistent definition of the exclusion region in our GCs. Decreasing the threshold resulted in only a marginal increase in the sample's stars that often exhibit poor photometric quality or are blends in the crowded central regions. Therefore, the adopted threshold represents a compromise between the number of stars and photometric reliability. The typical radius of the excluded circular region was 150 px (approximately 60 arcsec). This masking was applied after `DAOPHOT` processing to avoid degrading the PSF models of stars near the masked edges. Figure 1 illustrates the masking procedure, including the vignetting regions.

Since we are primarily interested in the scatter of the a versus $B-V$ dependence, we used only instrumental magnitudes of the stars to avoid propagating errors that might arise from the absolute calibration procedure. In addition, the data were not corrected for reddening. With this approach, there might be differences in zero points and slopes of the a versus $B-V$ dependencies compared to absolute calibrated and de-reddened data. However, a better-defined dependence is more important for our purpose than absolute values.

2.3. Gaia data and membership analysis

One of the crucial aspects of our study is the accurate distinction between field stars and clusters. To differentiate Milky Way field stars from GC members, we utilized astrometric data from the Gaia satellite (Gaia Collaboration 2016), specifically its third data release (DR3, Gaia Collaboration 2023). The Gaia space mission provides proper motions in equatorial coordinates, μ_α and μ^*_δ, as well as parallax measurements, ϖ, for hundreds of millions of objects (Gaia Collaboration 2023). In addition to astrometric measurements, Gaia also offers metrics to evaluate the quality of these measurements. These include `astrometric_excess_noise_sig`, `visibility_periods_used`, `ipd_frac_multi_peak`, and the re-normalized unit weight error (RUWE). Following the methodology of (Vasiliev & Baumgardt 2021), we applied specific criteria to assess data quality to determine cluster membership:

$$\mathrm{RUWE} < 1.4 \quad (1)$$

$$\texttt{astrometric\_excess\_noise\_sig} < 2 \quad (2)$$

$$\texttt{visibility\_periods\_used} > 12 \quad (3)$$

$$\texttt{ipd\_frac\_multi\_peak} < 2 \quad . \quad (4)$$

Furthermore, for each GC, we devised a specific selection criterion in both proper motion and magnitude dimensions to accurately represent their distributions within these parameter

spaces. The extent of the proper motion selection window was determined by the representation of the foreground and background field population and the distinctiveness of the cluster members relative to this background. For instance, in NGC 6541, the proper motion selection encompassed approximately $\mu_\alpha^{\rm clus} \pm 4$ and $\mu_\delta^{*\rm clus} \pm 4\,{\rm mas\,yr^{-1}}$. Conversely, for NGC 5904, this range expanded to about $\mu_\alpha^{\rm clus} \pm 20$ and $\mu_\delta^{*\rm clus} \pm 20\,{\rm mas\,yr^{-1}}$. Regarding the magnitude thresholds, for most clusters, we included stars up to $G = 21$ mag. However, for a select group of clusters (NGC 6401, NGC 4833, and NGC 6656), we applied a brighter limit of $G = 20$ mag. Additionally, a lower magnitude limit was set for NGC 6266 and at $G = 19$ mag. These differences do not reflect intrinsic properties of the clusters themselves, but are driven by observational considerations related to the density of foreground and background stars. For clusters located closer to the Galactic plane or bulge, the high density of non-member stars already provides a well-defined contamination component at brighter magnitudes, making deeper magnitude cuts unnecessary. In contrast, for more isolated halo clusters, a fainter magnitude limit is required to ensure a sufficient representation of the non-member population in the membership analysis. In extracting data from the Gaia catalogue, our queries were centred on each cluster, with the cone radius varied to include both cluster members and field stars in their immediate vicinity. To ensure comprehensive coverage, we used the angular scale radius, $R_{\rm scale}$, from (Vasiliev 2019), selecting stars within a radius of $3 \cdot R_{\rm scale}$ around each cluster.

The members of stellar clusters often aggregate in proper motion and parallax dimensions, yet distinguishing GC populations from field stars is not always straightforward. To quantitatively determine membership, we employed Gaussian mixture modelling in the proper motion and parallax parameter space, approximately following the method outlined in (Vasiliev 2019; Vasiliev & Baumgardt 2021). Further methodological specifics are elaborated in these referenced studies; here, our focus is on the underlying premise. We assume two components for each cluster: the cluster itself and external contamination. These components are characterized by their average proper motions and parallax ($\overline{\mu_\alpha}$, $\overline{\mu_\delta^*}$, and $\overline{\varpi}$), alongside their respective covariance matrices. The last included parameter represented a fraction between cluster members and contamination (field stars). In our parameter set, the last entry is specifically designed to express the fraction distinguishing cluster members from contaminating stars.

Although a parallax is included as one of the dimensions in the Gaussian mixture model, its discriminating power at typical GC distances is limited. In practice, the inclusion of a parallax leads primarily to a further purification of the member sample by down-weighting or removing a small number of obvious foreground or background stars. The resulting membership probabilities for the retained stars are therefore more robust, while the set of stars entering the a-photometry analysis and the conclusions presented in this work remain unaffected.

The motivation for retaining parallax in the model is to favour sample purity over completeness. Given that we focus on a small, peculiar population, minimizing contamination by foreground or background stars is more important than maximizing recall. Parallax is therefore used as an additional safeguard against obvious interlopers, even though its statistical weight is small compared to that of proper motions. Lastly, we note that eight of the eighteen clusters in our sample are located at heliocentric distances below ≈7 kpc, where parallax information can still assist in rejecting background contaminants, whereas for more distant clusters it primarily removes foreground stars with significant parallaxes.

Membership probabilities were derived using a Gaussian mixture model in the three-dimensional astrometric space $(\varpi, \mu_{\alpha*}, \mu_\delta)$. The model consists of one cluster component and one field component. The cluster is described by a mean parallax, $\bar{\varpi}_c$, a mean proper-motion vector $(\bar{\mu}_{\alpha*,c}, \bar{\mu}_{\delta,c})$, and intrinsic dispersions in parallax and proper motion, $(\sigma_{\varpi,c}, \sigma_{\mu_{\alpha*,c}}, \sigma_{\mu_{\delta,c}})$. The field population was modelled analogously, with mean astrometric parameters $\bar{\varpi}_f$ and $(\bar{\mu}_{\alpha*,f}, \bar{\mu}_{\delta,f})$, and their corresponding intrinsic dispersions $(\sigma_{\varpi,f}, \sigma_{\mu_{\alpha*,f}}, \sigma_{\mu_{\delta,f}})$. All astrometric components were convolved with the individual Gaia astrometric uncertainties. The last parameter reflects the fraction, η_c, of the cluster population. For the optimization of 13 parameters, we used SciPy library (Virtanen et al. 2020) to obtain preliminary estimates that served as an input into the MCMC routine implemented using the emcee library (Foreman-Mackey et al. 2013).

Initial parameter estimates were obtained using a maximum-likelihood optimization implemented in the `SciPy` library and subsequently refined using a Markov chain Monte Carlo (MCMC) approach with the `emcee` ensemble sampler. We employed 40 walkers and ran each chain for 4000 steps. Convergence was assessed using the integrated autocorrelation time estimated via the built-in `emcee` function `get_autocorr_time`. Based on these estimates, an initial burn-in phase was discarded, and the chains were thinned to obtain effectively independent posterior samples[3]. The resulting posterior distributions were used to derive membership probabilities for individual stars. An illustrative case of our analysis, featuring NGC 6541 with calculated membership probabilities for individual stars, is showcased in Fig. 2.

2.4. Stars selection

Including data of all stars in the *a*-photometry analysis would take into account the whole set of faint main sequence stars that have poor-quality photometry and red giant stars. Since the chemical peculiarity among main-sequence stars appears among slowly rotating hot stars ($T_{\rm eff} > 7000$ K Michaud et al. 1976) and was identified among stars from the extreme HB or blue HB regions, (E/B)HB, of GCs (Momany et al. 2020), we decided to limit our analysis to the regions of (E/B)HB and BS. If a star location significantly deviated from the typical CMD structures, but was close to the regions of interest, they were included in the sample because their position could signal some special behaviour (see the left panel of Fig. 3 for an example).

As is illustrated in Fig. 3, regions of interest were defined manually using clearly defined lines. For the general analysis, a strict division of the BS and (E/B)HB regions was not necessary. However, for further analysis of outliers, it might be interesting to look at the statistics of BS versus (E/B)HB candidates. In the majority of GCs, both groups of stars were clearly distinguished. Four specific cases of GCs without clearly defined HB and BS, including NGC 6273 (left panel of Fig. 3), are marked in Table 2.

3. The *a* photometry

It was discovered by Kodaira (1969) that CP stars exhibit a characteristic flux depression in several regions of the spectra (4100, 5200, and 6300 Å). To study 5200 Å region, a dedicated filter *g*2 centred on this wavelength (with FWHM 130 Å) was introduced by Maitzen (Maitzen 1998). This filter can be used for the cal-

[3] Using the example described here: https://emcee.readthedocs.io/en/stable/tutorials/monitor/

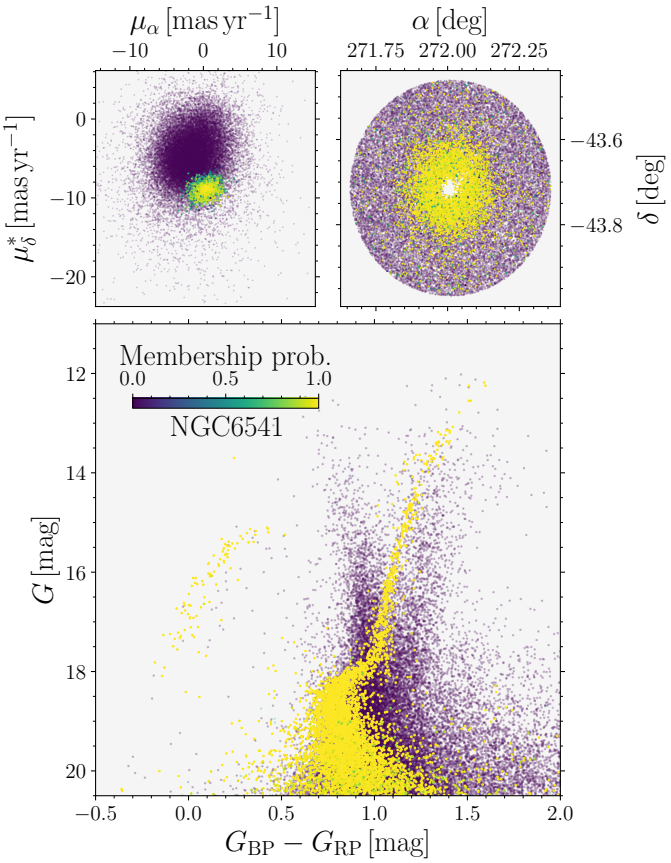

Fig. 2. Example of determined membership (colour-coded) for stars in NGC 6541. The top two panels depict the distribution of stars in proper motion space (left-hand plot) and equatorial coordinates (right-hand plot). The bottom panel shows a colour-magnitude diagram for NGC 6541 and its immediate area.

culation of the so-called a index (Maitzen 1976), which is used as a tool for identifying these CP stars (e.g. Cariddi et al. 2018; Netopil et al. 2007; Paunzen et al. 2014b).

We calculated the a index for each individual star in a particular GC as

$$a = g2 - \frac{B+V}{2}. \quad (5)$$

As was mentioned above, a photometry uses a $g2$ filter to analyse the characteristic flux depression region and it also employs two other filters to characterize the continuum of the star; for example, Johnson's B, V (our case) or b, y Strömgren filters or $g1$ Maitzen filter. As was shown by Paunzen et al. (2005), the method is particularly sensitive to CP2 and CP4 stars that clearly stand above the normality line in the a versus colour diagram (positive Δa), and to λ Boo stars that are located below the normality line (negative Δa) due to a deficiency of iron-peak elements.

3.1. Photometric quality handling based on a index

We derived the uncertainty of the a index via the error propagation law based on the used photometric B, V, $g2$ uncertainties. For each GC, we utilized the individual a-index uncertainties to check for the erroneous photometry within the sample. This was done by fitting the a-index error versus V magnitude dependency as shown in Fig. 4. The function used for data fitting was

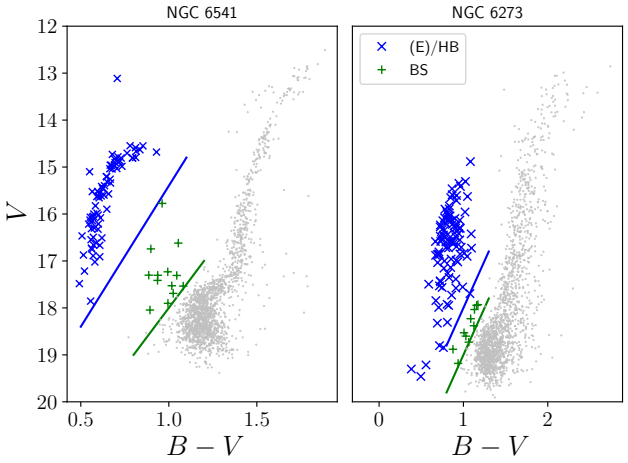

Fig. 3. CMDs of NGC 6541 (left) and NGC 6723 (right). In the case of NGC 6541, we can clearly distinguish BS (in green) and (E/B)HB (in blue) populations. For better visibility, the bottom border lines for BS and (E/B)HB regions are displayed in graphs. In the case of NGC 6273, we can see that the BS and HB are not clearly distinguished.

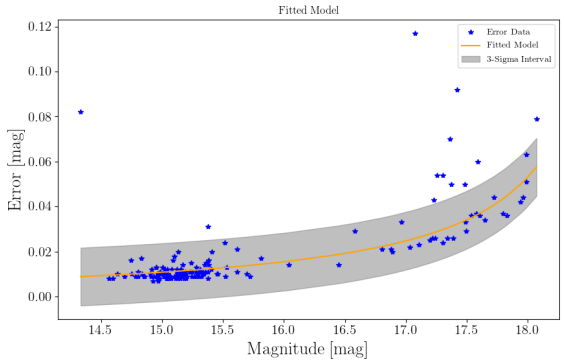

Fig. 4. a-index error versus the V magnitude for NGC 5272. The fit is shown with yellow line and the 3-sigma reliability interval is shown by the shaded grey region. Points lying outside the interval considered as having erroneous photometry were excluded from further analysis.

$f(m) = p_0 + p_1/(p_2 - m)$, where p_0, p_1, and p_2 are free parameters and m is the magnitude. The data were winsorized and the function was fitted by the least squares method to the data. The stars that had exceedingly large errors lying outside the 3σ interval were then removed from each GC's sample.

For the cleared sample, an a versus $B-V$ diagram was constructed for each of the GCs. This dependence was fitted with the normality line $a_0 = c_1 + c_2(B-V)$, where c_1 and c_2 are the intercept and slope, and the regions of the reliability interval were defined by 3σ.

Stars located outside the 3σ interval were marked as CP candidates (hereafter CPCs, red crosses in Fig. 5). We checked the location of every CPC in the cluster frame in order to avoid possible contamination that might produce an erroneous photometry. However, not a single case of such a star was identified. In addition, the known variable stars based on the catalogue by (Clement & collaborators 2001) were marked.

3.2. Test on the artificial data

When we compared our results with the work of (Paunzen et al. 2014a), who also searched for CPC in GCs, we noticed a difference. The slope of our fitted normality line is inverse to the

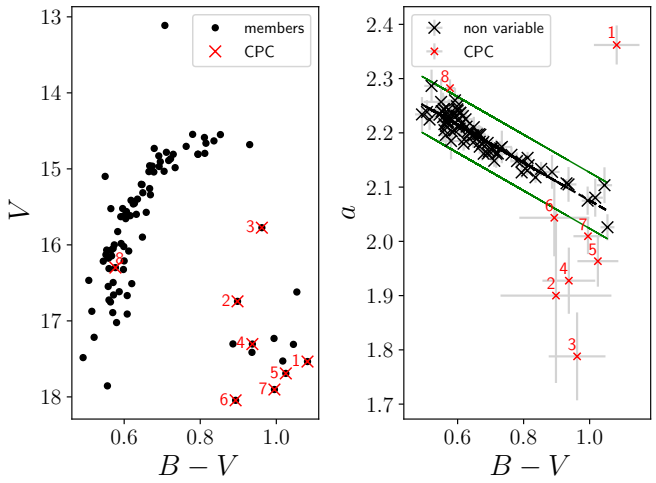

Fig. 5. CMDs of NGC 6541. The V vs. $B-V$ (left) and a vs. $B-V$ (right) diagrams of the region selected for analysis are shown. In both plots, there are CPC are marked with a colour and numbered. On the right-hand plot, we can see the fitted normality line in black and 3σ reliability intervals marked with green lines. It can be seen that there is no CPC among the variable stars in the cluster. In the left diagram, it can be seen that there is one CP candidate on the HB and most of them in the BS region of the cluster.

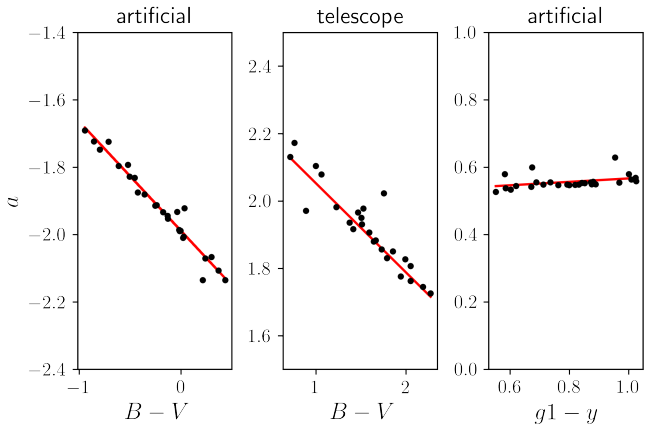

Fig. 6. Artificial and Danish telescope photometry results of selected stars of NGC 5024 (M53), using Johnsons's B, V and Strömgren $g1$ and y filters.

slope in the above-mentioned article. We claim that this discrepancy arises from the different filter sets used in the analyses. We employed the B and V filters, whereas they used the $g1$ and y filters. To test this assumption, we performed artificial photometry using available spectroscopic observations, adopting NGC 5024 (M53) as the test object.

To achieve this, we used spectroscopic data from the Large Sky Area Multi-Object Fibre Spectroscopic Telescope (LAMOST), also known as the 'Guo Shou Jing Telescope' (Cui et al. 2012). It is a reflecting Schmidt telescope with an effective aperture of 3.6–4.9 m, focal length of 20 m and 5° field of view (Wang et al. 1996). The data from LAMOST DR3[4] and DR5[5] were downloaded and processed.

Available LAMOST spectra of stars in the region were matched with stars in our sample. The total number of stars in common was 25. Then the artificial magnitudes for the Johnson filters B, V, Strömgren filter y, and Maitzen $g1$ and $g2$ were calculated by modelling the filter spectral-sensitivity profiles and by integrating the spectral intensity of the star through them. Spectral profiles of filters were taken from the Asiago Database on Photometric Systems (Fiorucci & Munari 2003); (Moro & Munari 2000).

From Fig. 6, we can see that the slope of the dependence is negative when using B and V filters, while the slope is positive when using y and Maitzen $g1$. Although the agreement between the slopes of the artificial and observed data is not perfect (-0.325 for artificial data and -0.254 for the measured ones), the general trend is very well preserved (see the left and middle panel of Fig. 6). When Strömmgren filters are used, the result is a positive slope of 0.051 in line with (Paunzen et al. 2014a). Thus, we consider our approach to be correct. The difference between the artificial and the data obtained by the Danish telescope is likely caused by the contamination of the spectra with nearby stars (as the angular resolution of one fibre in LAMOST is ~3.3 arcsec) or by the observing conditions.

4. Results and discussion

4.1. Statistics of the CPC

As was described in Sect. 3, we identified CPCs in each of the GCs and obtained the numbers and percentage of CPC at (E/B)HB and BS stars. The full results for all GCs in our sample can be seen in Table 2. On average, if present, CPCs represent 4.2% of the stars in the sample. The number of stars on (E/B)HB and BS regions for each GC varied from 27 (NGC 6397) to 259 (NGC 5024). There is no obvious correlation between the number of stars available in a particular GC and the number or percentage of CPCs that could signal a possible bias or artificial effect linked with the quality of photometry or with the size of a GC.

The CPCs identified in Sect. 3 and listed in Appendices A and B are well separated from their neighbouring stars and have photometric errors comparable with other stars. Thus, we can reject the notion that they lie outside of the normality lines due to contamination or poor photometry. Some of these outliers lie close to the 3σ limit and should only be considered as weak candidates. On the other hand, there are distinct outliers indicating strong CPCs; for example, in NGC 4833 (Fig. A.4).

The most CPCs in our dataset were detected in NGC 5272 represented by 11 stars out of 145, which is 7.6% of the stars analysed in this GC. The majority of CPCs were found among BS stars (9 stars). This GC with a metallicity of -1.5 (Carretta et al. 2009) and age estimate of 11.75 Gyrs (VandenBerg et al. 2013) claims no extreme in our data.

On the other hand, not a single CPC was found in four clusters of a Galactic bulge origin: NGC 6121, NGC 6218, NGC 6388, and NGC 6397. Two of these clusters are the oldest in our sample (13 Gyrs), and both of them seem to originate in the Galactic disc (Massari et al. 2019). Finding no CPC could mean that the CPC migrated to the central regions due to dynamical effects (Lanzoni et al. 2016), where they were undetectable for us, or that there are not conditions for CP stars to emerge. In the cases of NGC 6397 and NGC 6121, the non-detection could simply emerge from a low number of available stars.

[4] http://dr3.lamost.org/
[5] https://dr5.lamost.org/

Table 2. Statistics of identified CPCs.

NGC	HB	Total	CPC	%	Sep	HBc	BSc	HBc%	BSc%	Sig	*p*-val	OR
1851	yes	98	7	7.1	yes	2	5	29	71	yes	$p < 0.001$	35
2808	no	163	2	1.2	no	1	1	50	50	–	–	–
3201	yes	100	2	2.0	yes	1	1	50	50	–	–	–
4833	yes	110	5	4.5	yes	2	3	40	60	yes	0.002	38
5024	yes	259	7	2.7	yes	3	4	43	57	yes	0.002	14
5272	yes	145	11	7.6	yes	2	9	18	82	yes	0.002	29
5904	yes	90	1	1.1	yes	0	1	0	–	–	–	–
6121	yes	41	0	0	yes	0	0	0	0	–	–	–
6218	yes	85	0	0	yes	0	0	0	0	–	–	–
6254	yes	87	2	2.3	no	0	2	0	100	–	–	–
6266	yes	128	6	4.6	no	4	2	67	33	yes	0.002	15
6273	yes	103	6	5.8	no	2	4	33	67	yes	$p < 0.001$	94
6388	no	206	0	0	yes	0	0	0	0	–	–	–
6397	yes	27	0	0	yes	0	0	0	0	–	–	–
6402	yes	194	8	4.1	yes	8	0	100	0	no	1	–
6541	yes	84	3	3.6	yes	1	2	33	67	yes	0.023	35
6656	yes	132	8	6.1	yes	2	6	25	75	yes	$p < 0.001$	22
6723	yes	90	3	3.3	yes	0	3	0	100	yes	$p < 0.001$	65

Notes. Columns are marked in the following way. NGC: Number of the studied object in the NGC catalogue. HB: Gives information if there is a complete HB in our CMD data. Total: Total number of stars in BS and (E/B)HB taken for analysis. CPC: Number of all CP stars candidates in the cluster. %: Percentage of CP candidates in the analysed sample. Sep: Population of clearly distinguished BS and (E/B)HB stars. HBc: Number of HB candidates. BSc: Number of BS candidates. HBc%: Percentage of the CPC on the HB. BSc%: Percentage of CPC in the BS region. Sig: Says if the data were marked as statistically significant in Fisher's test of the data. p-val: Probability of obtaining the observed distribution assuming independence between CPC occurrence and stellar type. OR: Odds ratio for the statistically significant cases, meaning how much more likely the CPC star is to be a BS member than HB.

As we show in Fig. 7, there is no correlation in the data between age and the percentage of the CPC. If we search for a correlation between age or metallicity and the CPC percentage, we find no correlation (Pearson correlation coefficient R of −0.15 and −0.24). Due to a significant inhomogeneity in the clusters' origins (the highest number of GCs with the same origin is five), we are not able to come to a conclusion about a correlation between the CPC percentage and the estimated dynamical association of the clusters.

NGC 2808 and NGC 6388 do not have complete HBs in our data as we cannot see the main-sequence turn-off point in their CMD. However, it seems that the vast majority of the HB is present in the sample (see Appendix A). Although our analysis might be incomplete, we left these GCs in our sample and counted them in the statistics. No CPC was found among known variable stars.

4.2. Evolutionary status of CPC

The major fraction of CPCs – 10 out of 14 GCs with CPCs – are located among BS stars. In three cases, the CPC population consists fully of BS stars, and the percentage of BS was less than 60% in only four cases. On the other hand, we found no BS CPC candidate in one of our GCs. To examine whether the observed larger amount of CPCs among BS stars could arise by chance, we applied Fisher's exact test (Fisher 1922) to 2×2 contingency tables constructed for each GC. The tables classified stars by CPC status (CPC or non-CPC) and stellar type (BS or non-BS). The null hypothesis assumes that CPC occurrence is independent of stellar type. Statistical significance was assessed at a standard value of $p < 0.05$. In addition, the odds ratio (OR) was calculated to quantify the strength of the association, indicating how much more a BS star is likely to be classified as a CPC compared to non-BS (HB) stars (see Table 2). We performed this test on GCs with more than two CPCs. In 9 out of 14 GCs hosting CPCs, Fisher's exact test indicates a statistically significant association, with BS stars showing higher odds of being CPCs. In the remaining clusters, no significant association was detected due to small sample sizes. These results suggest that the observed trend of BS being CPC is unlikely to be due to chance and that there could be a connection between chemical peculiarity and BS stars.

Blue stragglers are found everywhere in our galaxy – in the field, in open clusters, and in GCs. There are multiple scenarios for BS origin, as discussed in (Ahumada & Lapasset 2007): mass transfer in binary systems, stellar mergers and direct collisions, the non-standard internal mixing mechanism, or formation later than the bulk system. Binary mass transfer is considered the most common way in which BSs originate in low-density systems. Collisions are thought to be most common way for high-density systems such as GCs.

Da Costa et al. (1986) inspected spectra of six BS stars of NGC 5139 (ω Cen) and found no abnormalities. However, there are cases of chemical abnormalities having been found in BS stars of GCs. Significant C/O depletion was found in a fraction of NGC 104 BS stars by (Ferraro et al. 2006), caused most probably by mass transfer in binary systems. In the report of (Lovisi 2014), there is evidence suggestive of radiative levitation in some BS stars of NGC 6397 and NGC 6752, as well as O or C/O depletion of several BS stars suggested as a result of mass transfer, in NGC 7099. (Lovisi et al. 2012) studied BS and HB stars in GC 6397. They found a deviations of iron abundance among hot HB and BS stars varying from the mean estimated value for the cluster. This discrepancy was interpreted by the authors as a result of metal radiative levitation, occurring in stars with shallow or no convective envelopes. It is worth noting that we did not detect a single CPC in NGC 6397.

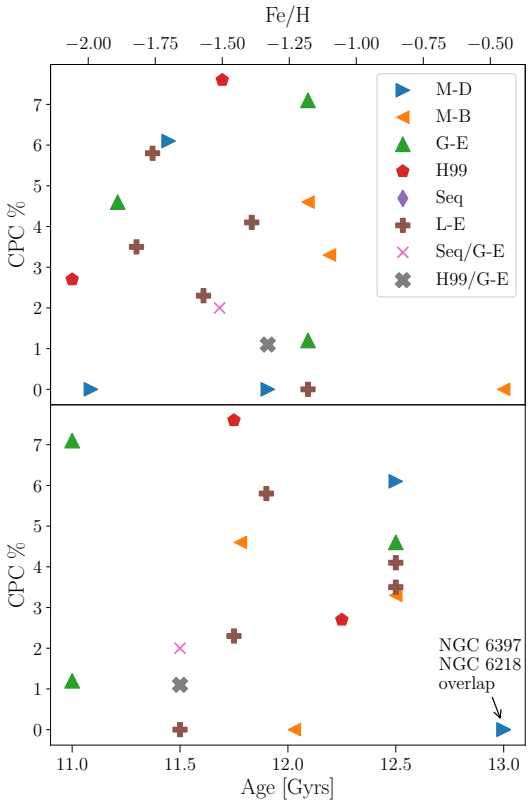

Fig. 7. CPC percentage as a function of age and metallicity for our 18 GCs sample with respect to dynamical association of the clusters as estimated by (Massari et al. 2019). Abbreviations in this column were adopted from the above-mentioned work as follows: M-D for Main-Disc; M-B for Main-Bulge; G-E for Gaia-Enceladus; H99 for Helmi Streams; Seq for Sequoia galaxy; and L-E for clusters unassociated with any of the stellar streams but exhibiting low energy.

Metallic levitation is connected to the CP phenomenon (Michaud 1970), and we might argue that the conditions for the CP phenomenon or other chemical abnormality to arise are present in GCs. As was discussed earlier in this section, chemical peculiarity seems to appear preferentially among BSs (see the figures in Appendix A). In our data, some of the CPCs are located slightly above the normality line, suggesting that some of them might be similar to CP2 or CP4 stars. However, most of CPCs are located below the normality line, which means that they might be more metal-deficient than other stars in the cluster and that similar effects to λ Boo stars might appear among BSs. For chemical peculiarity to emerge, a stable radiative envelope and slow to moderate rotation (<≈100 km/s), where the rotational mixing is weak, are the necessary ingredients (Abt & Morrell 1995).

Ferraro et al. (2023) studied 320 stars in eight GCs and found that most BSs (73%) are relatively slow rotators with $v \sin i < 40$ km/s (preferentially in high-density GCs) although there might be very fast rotators exceeding $v \sin i \approx 200$ km/s (preferentially in loose clusters). Thus, the first condition for CP2 type peculiarity is met. The second condition – a strong, stable, and long-lasting globally organized magnetic field – is predicted for BSs that formed through the merger channel (Schneider et al. 2016, 2020; Ryu et al. 2025) and has been observed in some BSs (for example, τ Sco, Donati et al. 2006). The same way of forming strong magnetic fields is considered as one of the possible channels in main-sequence CP stars (e.g., Ferrario et al. 2009; Tutukov & Fedorova 2010). Thus, detecting CP2 type chemical peculiarity among BSs may represent strong support for the merger scenario of forming CP2 stars and identify BSs that formed via merging.

Nevertheless, most of the BS CPCs are similar to λ Boo stars and can be their old-population analogues. The lower metallicity can point towards the mass transfer scenario of forming a BS, which is also one of the proposed scenarios for the formation of λ Boo stars (Paunzen 1998). Finding both types of these possible CP stars in GCs shows that the formation of BS stars is complex and is probably possible in multiple ways. A larger number of metal poor CPCs might suggest that in GCs the formation via mass transfer is dominant.

5. Conclusions and future prospects

We gathered photometric observations of 18 Milky Way GCs using the Danish 1.54 m telescope at La Silla observatory, Chile. The observations were carried out in the B, V, and $g2$ filters in order to perform a photometry that is sensitive to the chemical peculiarity of stars with strong magnetic fields. We limited ourselves to bright hot stars located in (E/B)HB and BS regions that have good-quality data and where we can expect chemical peculiarity to emerge.

We identified the CPCs in 14 out of 18 studied GCs. The fraction of CPCs ranges from 1% to 7%, depending on the individual cluster. We found no correlation between the incidence rate of CPCs and cluster parameters such as metallicity, age, or origin. This suggests that the distribution of CPCs in GCs is likely random.

In 10 of the 14 GCs with identified CPCs, the majority of the CPC population consists of BSs. This indicates that the chemical peculiarity appears to be predominantly present in BSs in GCs. In addition, our findings suggest that BSs CPCs seem to be more metal-poor than the other stars in a given GC, which may point towards the prevalence of the mass transfer scenario in forming BSs in GCs.

Acknowledgements. MŠ and MS acknowledge the MŠMT Inter Transfer project LTT20015, This work has made use of data from the European Space Agency (ESA) mission *Gaia* (`https://www.cosmos.esa.int/gaia`), processed by the *Gaia* Data Processing and Analysis Consortium (DPAC, `https://www.cosmos.esa.int/web/gaia/dpac/consortium`). Funding for the DPAC has been provided by national institutions, in particular the institutions participating in the *Gaia* Multilateral Agreement. This research made use of the following Python packages: `Astropy` (Astropy Collaboration 2013, 2018, 2022), `dustmaps` (Green 2018), `emcee` (Foreman-Mackey et al. 2013), `IPython` (Pérez & Granger 2007), `Matplotlib` (Hunter 2007), `NumPy` (Harris et al. 2020), and `SciPy` (Virtanen et al. 2020).

References

Abt, H. A., & Morrell, N. I. 1995, ApJS, 99, 135
Ahumada, J. A., & Lapasset, E. 2007, A&A, 463, 789
Astropy Collaboration (Robitaille, T. P., et al.) 2013, A&A, 558, A33
Astropy Collaboration (Price-Whelan, A. M., et al.) 2018, AJ, 156, 123
Astropy Collaboration (Price-Whelan, A. M., et al.) 2022, ApJ, 935, 167
Baumgardt, H., Sollima, A., Hilker, M., et al. 2023, Fundamental Parameters of Galactic Globular Clusters, `https://people.smp.uq.edu.au/HolgerBaumgardt/globular/`
Behr, B. B., Cohen, J. G., McCarthy, J. K., & Djorgovski, S. G. 1999, ApJ, 517, L135
Bernhard, K., Hümmerich, S., Otero, S., & Paunzen, E. 2015, A&A, 581, A138
Braithwaite, J., & Spruit, H. C. 2004, Nature, 431, 819
Cariddi, S., Azatyan, N. M., Kurfürst, P., et al. 2018, New Astron., 58, 1
Carretta, E., Bragaglia, A., Gratton, R., D'Orazi, V., & Lucatello, S. 2009, A&A, 508, 695

Ceccarelli, E., Mucciarelli, A., Massari, D., Bellazzini, M., & Matsuno, T. 2024, A&A, 691, A226
Clement, C. M., & collaborators. 2001, Catalogue of Variable Stars in Galactic Globular Clusters, http://www.astro.utoronto.ca/~cclement/cat/listngc.html, version updated regularly
Cui, X.-Q., Zhao, Y.-H., Chu, Y.-Q., et al. 2012, Res. Astron. Astrophys., 12, 1197
Da Costa, G. S., Norris, J., & Villumsen, J. V. 1986, ApJ, 308, 743
Davis, L. E. 1994, A Reference Guide to the IRAF/DAOPHOT Package, https://iraf.net/irafdocs/daorefman.pdf
Donati, J. F., Howarth, I. D., Jardine, M. M., et al. 2006, MNRAS, 370, 629
Ferrario, L. 2018, CAOSP, 48, 15
Ferrario, L., Pringle, J. E., Tout, C. A., & Wickramasinghe, D. T. 2009, MNRAS, 400, L71
Ferraro, F. R., Sabbi, E., Gratton, R., et al. 2006, ApJ, 647, L53
Ferraro, F. R., Mucciarelli, A., Lanzoni, B., et al. 2023, Nat. Commun., 14, 2584
Fiorucci, M., & Munari, U. 2003, A&A, 401, 781
Fisher, R. A. 1922, J. R. Stat. Soc., 85, 87
Forbes, D., & Bridges, T. 2010, MNRAS, 404, 1203
Foreman-Mackey, D., Hogg, D. W., Lang, D., & Goodman, J. 2013, PASP, 125, 306
Frommert, H., & Kronberg, C. 2019, Milky Way Globular Clusters, http://www.messier.seds.org/xtra/supp/mw_gc.html
Gaia Collaboration (Prusti, T., et al.) 2016, A&A, 595, A1
Gaia Collaboration (Vallenari, A., et al.) 2023, A&A, 674, A1
Ghazaryan, S., & Alecian, G. 2016, MNRAS, 460, 1912
Gratton, R. G., Carretta, E., & Bragaglia, A. 2012, A&ARv, 20, 50
Gray, R. O. 1988, AJ, 95, 220
Green, G. M. 2018, JOSS, 3, 695
Harris, C. R., Millman, K. J., van der Walt, S. J., et al. 2020, Nature, 585, 357
Hroch, F. 2014, Astrophysics Source Code Library [record ascl:1402.006]
Hümmerich, S., Paunzen, E., & Bernhard, K. 2020, A&A, 640, A40
Hunter, J. D. 2007, Comput. Sci. Eng., 9, 90
Johnson, H. L., & Morgan, W. W. 1953, ApJ, 117, 313
Kodaira, K. 1969, ApJ, 157, L59
Krtička, J., Marková, H., Mikulášek, Z., et al. 2013, A&A, 556, A18
Lanzoni, B., Ferraro, F. R., Alessandrini, E., et al. 2016, ApJ, 833, L29
Lovisi, L. 2014, MmSAI, 85, 283
Lovisi, L., Mucciarelli, A., Lanzoni, B., et al. 2012, ApJ, 754, 91
Maitzen, H. M. 1976, A&A, 51, 223
Maitzen, H. M. 1998, HvaOB, 22, 83
Maitzen, H. M., Pressberger, R., & Paunzen, E. 1998, A&AS, 128, 573
Massari, D. 2025, Res. Notes Am. Astron. Soc., 9, 64
Massari, D., Koppelman, H. H., & Helmi, A. 2019, A&A, 630, 8
Michaud, G. 1970, ApJ, 160, 641
Michaud, G., Charland, Y., Vauclair, S., et al. 1976, ApJ, 210, 447
Michaud, G., Megessier, C., & Charland, Y. 1981, A&A, 103, 244
Michaud, G., Tarasick, D., Charland, Y., & Pelletier, C. 1983, ApJ, 269, 239
Michaud, G., Richer, J., & Richard, O. 2008, ApJ, 675, 1223
Milone, A. P., & Marino, A. F. 2022, Universe, 8, 359
Moffat, A. F. J. 1969, A&A, 3, 455
Momany, Y., Zaggia, S., Montalto, M., et al. 2020, Nat. Astron., 4, 1092
Moro, D., & Munari, U. 2000, A&A, 147, 361
Netopil, M., Paunzen, E., Maitzen, H. M., et al. 2007, A&A, 462, 591
Pace, G., Recio-Blanco, A., Piotto, G., & Momany, Y. 2006, A&A, 452, 493
Paunzen, E. 1998, CAOSP, 27, 395
Paunzen, E., Stütz, C., & Maitzen, H. M. 2005, A&A, 441, 631
Paunzen, E., Iliev, I. K., Pintado, O. I., et al. 2014a, MNRAS, 443, 2492
Paunzen, E., Netopil, M., Maitzen, H. M., et al. 2014b, A&A, 564, A42
Pérez, F., & Granger, B. E. 2007, Comput. Sci. Eng., 9, 21
Piatti, A. E., & Carballo-Bello, J. A. 2020, A&A, 637, L2
Preston, G. W. 1974, ARA&A, 12, 257
Ryu, T., Sills, A., Pakmor, R., de Mink, S., & Mathieu, R. 2025, ApJ, 980, L38
Schneider, F. R. N., Podsiadlowski, P., Langer, N., Castro, N., & Fossati, L. 2016, MNRAS, 457, 2355
Schneider, F. R. N., Ohlmann, S. T., Podsiadlowski, P., et al. 2019, Nature, 574, 211
Schneider, F. R. N., Ohlmann, S. T., Podsiadlowski, P., et al. 2020, MNRAS, 495, 2796
Stetson, P. B. 1987, PASP, 99, 191
Stibbs, D. W. N. 1950, MNRAS, 110, 395
Tailo, M., Di Criscienzo, M., D'Antona, F., Caloi, V., & Ventura, P. 2016, MNRAS, 457, 4525
Thompson, R. 2005, PASP, 347, 29
Tutukov, A. V., & Fedorova, A. V. 2010, Astron. Rep., 54, 156
VandenBerg, D. A., Brogaard, K., Leaman, R., & Casagrande, L. 2013, AJ, 134, 47
Vasiliev, E. 2019, MNRAS, 484, 2832
Vasiliev, E., & Baumgardt, H. 2021, MNRAS, 505, 5978
Virtanen, P., Gommers, R., Oliphant, T. E., et al. 2020, Nat. Methods, 17, 261
Wang, S.-G., Su, D.-Q., Chu, Y.-Q., Cui, X., & Wang, Y.-N. 1996, Appl. Opt., 35, 5155

Appendix A: CMDs of our sample's GCs

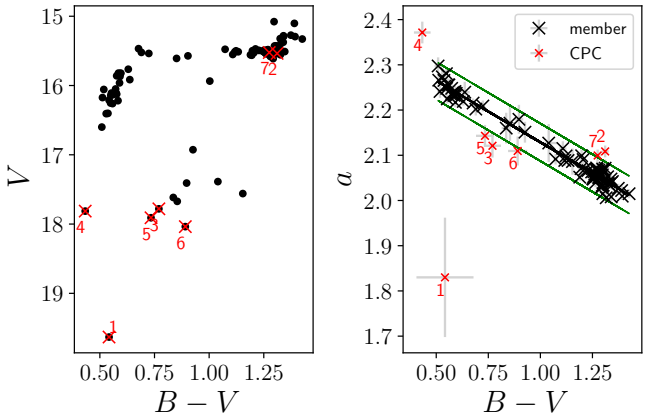

Fig. A.1. CMD of NGC 1851.

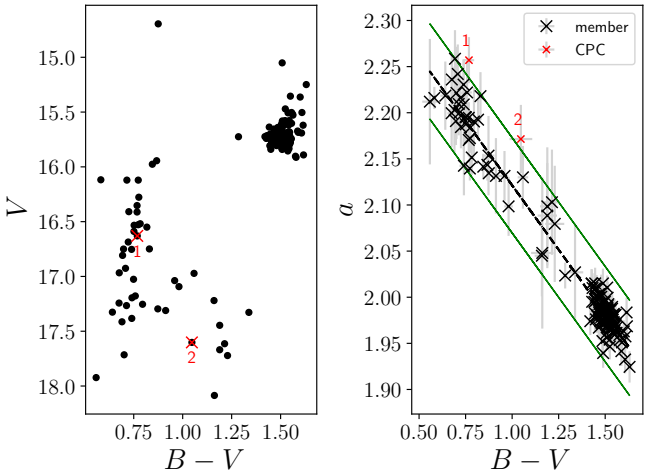

Fig. A.2. CMD of NGC 2808.

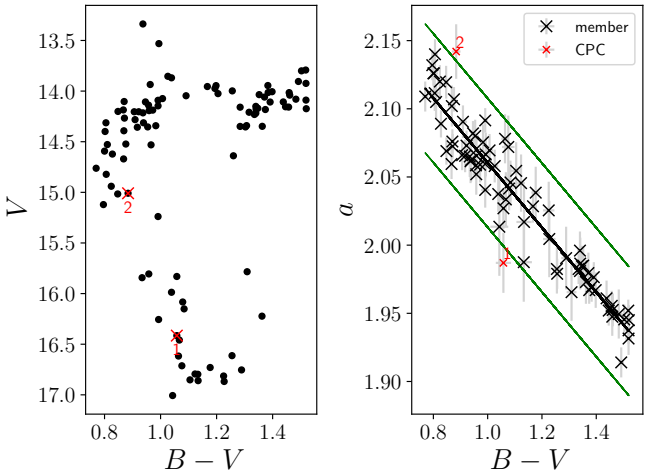

Fig. A.3. CMD of NGC 3201.

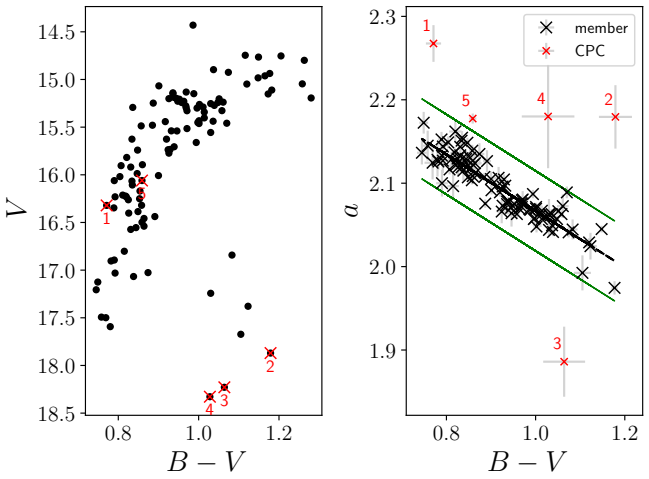

Fig. A.4. CMD of NGC 4833.

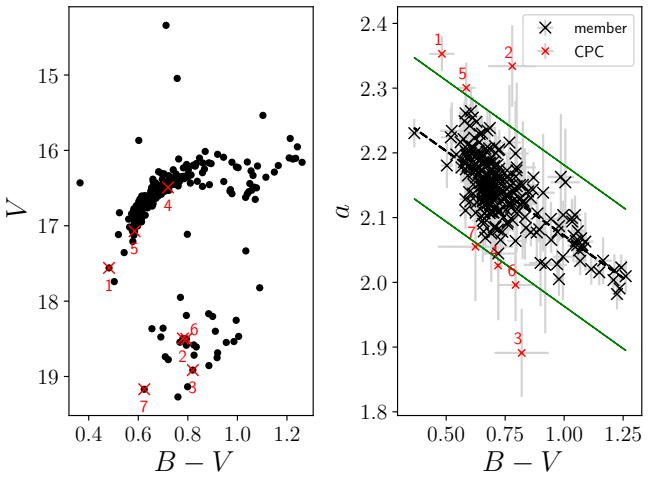

Fig. A.5. CMD of NGC 5024.

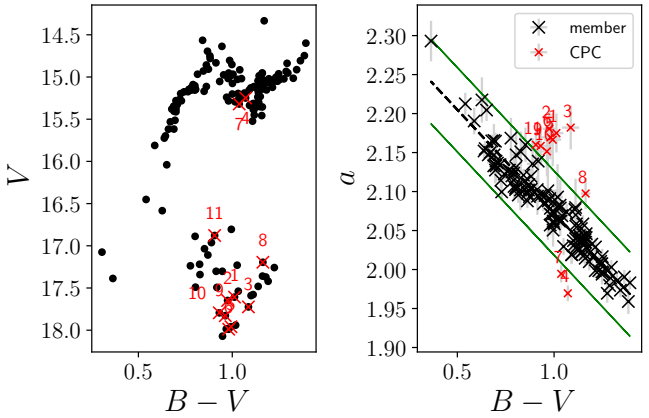

Fig. A.6. CMD of NGC 5272.

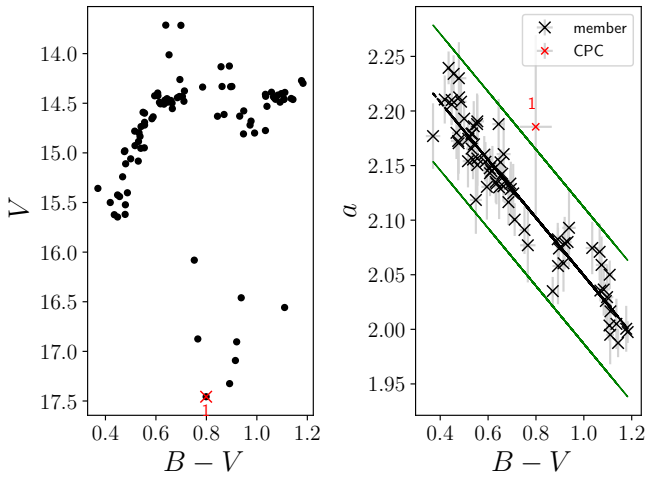

Fig. A.7. CMD of NGC 5904.

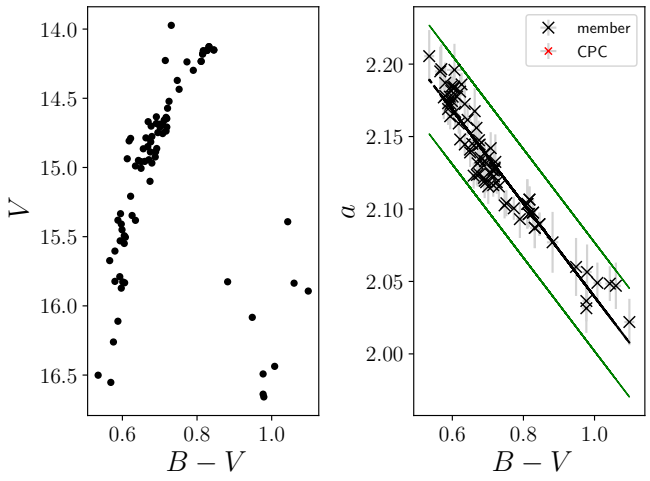

Fig. A.8. CMD of NGC 6218.

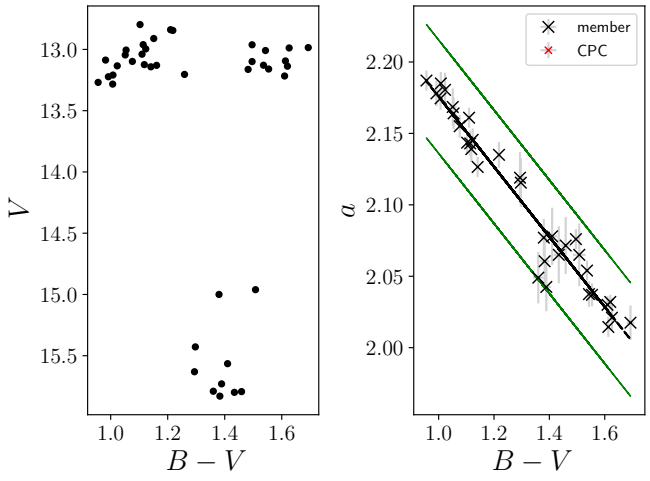

Fig. A.9. CMD of NGC 6121.

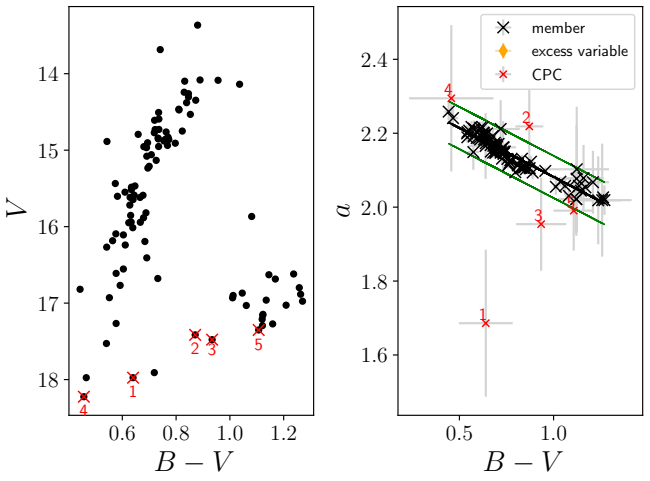

Fig. A.10. CMD of NGC 6254.

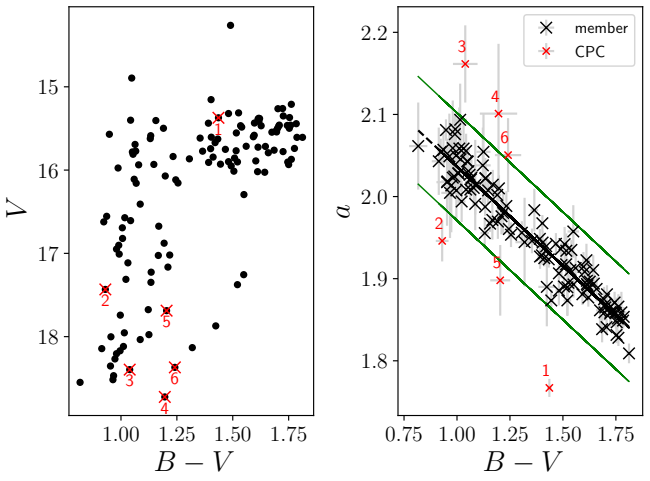

Fig. A.11. CMD of NGC 6266.

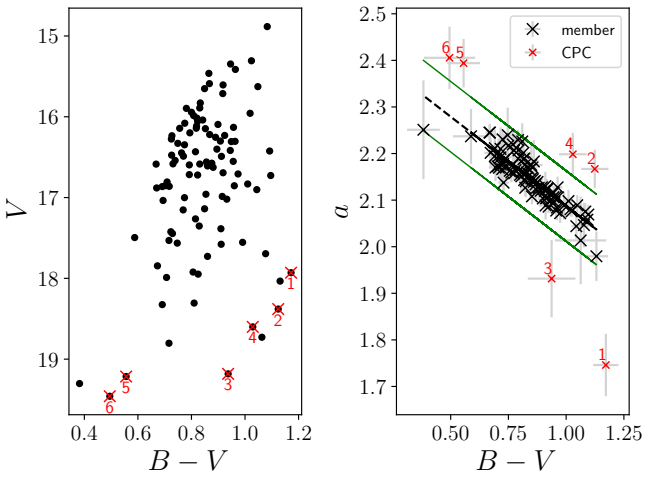

Fig. A.12. CMD of NGC 6273.

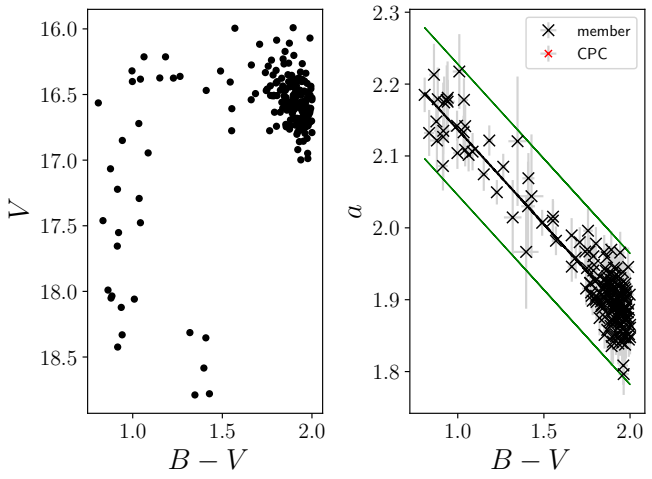

Fig. A.13. CMD of NGC 6388.

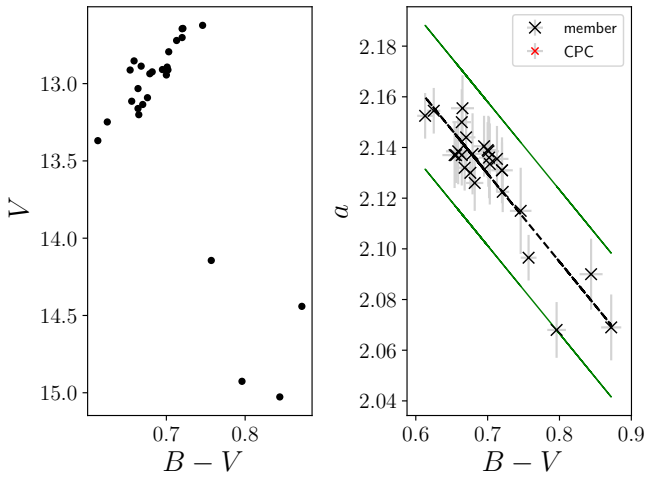

Fig. A.14. CMD of NGC 6397.

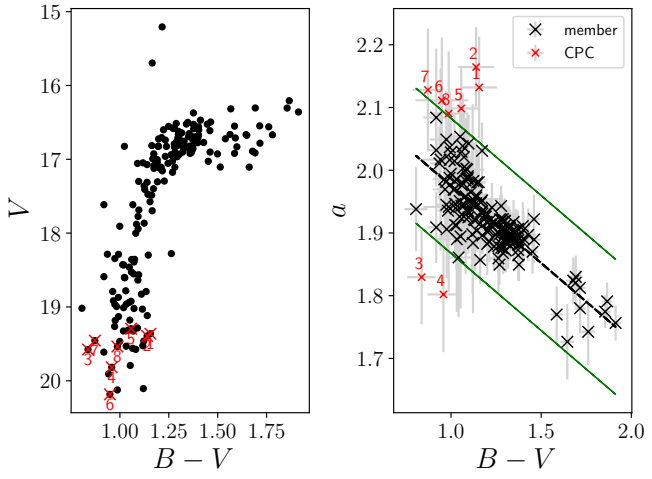

Fig. A.15. CMD of NGC 6402.

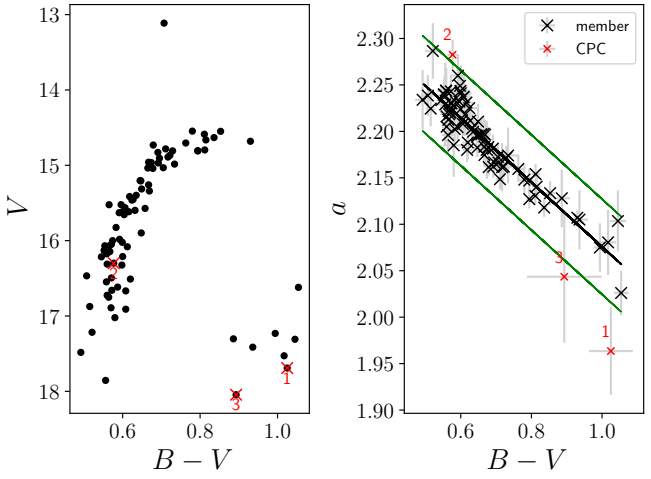

Fig. A.16. CMD of NGC 6541.

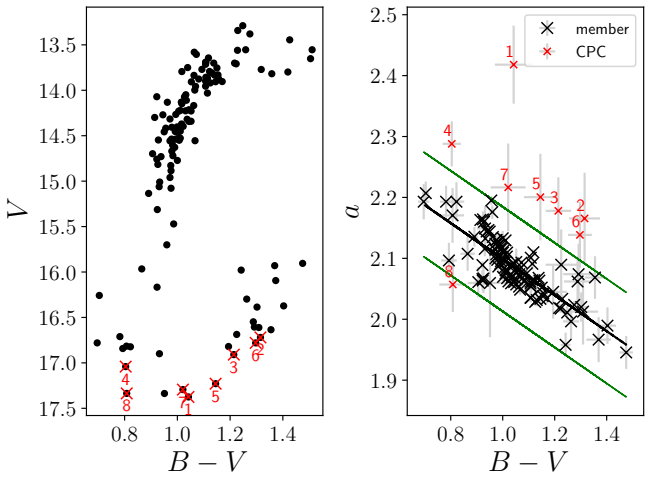

Fig. A.17. CMD of NGC 6656.

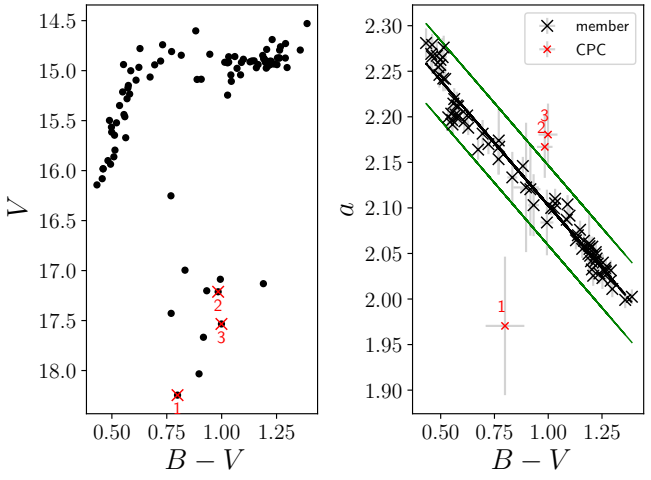

Fig. A.18. CMD of NGC 6723.

Appendix B: Lists of CPC stars for each GC in our sample

Table B.1. Coordinates of CPC stars in NGC 1851.

Number	RA	DEC
1	05:13:56.00	-40:02:30.08
2	05:14:09.72	-40:01:55.88
3	05:14:27.36	-40:01:12.18
4	05:14:16.26	-40:01:56.24
5	05:14:17.34	-39:59:35.30
6	05:14:20.54	-40:03:34.85
7	05:14:13.43	-40:03:01.91

Table B.2. Coordinates of CPC stars in NGC 2808.

Number	RA	DEC
1	09:11:47.46	-64:51:56.70
2	09:12:46.62	-64:48:40.72

Table B.3. Coordinates of CPC stars in NGC 3201.

Number	RA	DEC
1	10:17:42.81	-46:30:01.22
2	10:17:55.20	-46:28:29.21

Table B.4. Coordinates of CPC stars in NGC 4833.

Number	RA	DEC
1	12:59:59.60	-70:50:05.03
2	12:59:33.36	-70:49:58.58
3	12:59:11.29	-70:50:39.95
4	12:59:10.00	-70:53:47.72
5	13:00:03.88	-70:57:12.78

Table B.5. Coordinates of CPC stars in NGC 5024.

Number	RA	DEC
1	13:12:51.06	+18:10:04.30
2	13:12:53.51	+18:09:15.44
3	13:12:41.47	+18:11:41.21
4	13:13:07.73	+18:14:19.28
5	13:12:55.24	+18:11:12.95
6	13:12:52.75	+18:04:58.19
7	13:12:44.82	+18:10:40.19

Table B.6. Coordinates of CPC stars in NGC 5272.

Number	RA	DEC
1	13:41:50.26	+28:20:42.76
2	13:41:49.84	+28:23:32.68
3	13:41:49.83	+28:25:17.26
4	13:42:24.37	+28:24:21.92
5	13:41:52.10	+28:23:32.14
6	13:42:29.25	+28:18:40.10
7	13:42:04.39	+28:23:35.59
8	13:42:23.51	+28:27:27.32
9	13:42:06.01	+28:18:20.16
10	13:42:35.16	+28:23:16.98
11	13:41:57.08	+28:26:45.24

Table B.7. Coordinates of CPC stars in NGC 5904.

Number	RA	DEC
1	15:18:22.45	+02:01:24.64

Table B.8. Coordinates of CPC stars in NGC 6254.

Number	RA	DEC
1	16:57:00.42	-04:01:39.90
2	16:57:04.36	-04:00:27.18

Table B.9. Coordinates of CPC stars in NGC 6266.

Number	RA	DEC
1	17:00:58.95	-30:08:36.10
2	17:00:59.66	-30:05:10.28
3	17:01:06.06	-30:11:12.66
4	17:01:03.01	-30:03:32.62
5	17:01:18.12	-30:05:24.07
6	17:01:17.67	-30:09:42.34

Table B.10. Coordinates of CPC stars in NGC 6273.

Number	RA	DEC
1	17:02:40.94	-26:20:21.41
2	17:02:16.69	-26:13:12.36
3	17:02:31.15	-26:20:05.03
4	17:02:51.25	-26:16:56.24
5	17:02:32.08	-26:21:04.39
6	17:02:28.24	-26:11:21.80

Table B.11. Coordinates of CPC stars in NGC 6402.

Number	RA	DEC
1	17:37:44.45	-03:14:04.99
2	17:37:55.84	-03:16:30.50
3	17:37:42.25	-03:19:41.84
4	17:37:27.65	-03:11:54.17
5	17:37:51.09	-03:17:11.58
6	17:37:32.67	-03:17:45.92
7	17:37:34.23	-03:12:02.59
8	17:37:42.03	-03:12:50.69

Table B.12. Coordinates of CPC stars in NGC 6541.

Number	RA	DEC
1	18:07:47.21	-43:44:31.52
2	18:07:52.09	-43:42:42.01
3	18:08:04.99	-43:40:53.26

Table B.13. Coordinates of CPC stars in NGC 6656.

Number	RA	DEC
1	18:36:02.19	-23:53:24.97
2	18:36:30.03	-23:55:48.43
3	18:36:24.78	-23:49:31.08
4	18:36:10.17	-23:54:37.58
5	18:36:11.37	-23:58:06.02
6	18:36:15.86	-23:58:21.83
7	18:36:37.77	-23:51:22.57
8	18:36:40.77	-23:52:33.35

Table B.14. Coordinates of CPC stars in NGC 6723.

Number	RA	DEC
1	18:59:21.71	-36:36:34.56
2	18:59:30.47	-36:39:21.92
3	18:59:29.36	-36:39:33.55